Surface deformation and coherence measurements of Kilauea Volcano, Hawaii from SIR-C radar interferometry

P. A. Rosen, S. Hensley, H. A. Zebker[1], F. H. Webb, and E. Fielding
Jet Propulsion Laboratory, California Institute of Technology, Pasadena, California

Received _____—; accepted —..—_ __._-_ . . ..._

Submitted to the *Journal of Geophysical Research*, October 20, 1995.

Short title: SIR-C INTERFEROMETRY AT KILAUEA, HAWAII

[1] Presently at Electrical Engineering and Geophysics Departments, Stanford University, Stanford, California

Abstract.

The SIR-C/X-SAR radar on board the space shuttle Endeavor imaged Kilauea Volcano, Hawaii in April and October 1994 for the purpose of measuring active surface deformation by the methods of repeat-pass differential radar interferometry. Observations at 24 cm (L-band) and 5.6 cm (C-band) wavelengths were reduced to interferograms showing apparent surface deformation over the six month interval and over a succession of one day intervals in October, A statistically significant local phase signature in the six-month interferogram is coincident with the Pu'u O'o lava vent. Interpreted as deformation, the signal implies cm-scale deflation in an area several kilometers wide surrounding the vent. Peak deflation is roughly 14 cm if the deformation is purely vertical, centered southward of the Pu'u O'o caldera. Delays in the radar signal phase induced by atmospheric refractivity anomalies introduce spurious apparent deformation signatures, at the level of 12 cm peak-to-peak in the radar line-of-sight direction. Though the phase observations are suggestive of the wide-area deformation measured by GPS methods, the atmospheric effects are large enough to limit the interpretation of the result. It is difficult to characterize cm-scale deformations spatially distributed over tens of kilometers using differential interferometry without supporting simultaneous, spatially distributed measurements of refractivity along the radar line-of-sight.

Studies of the interferometric correlation of images acquired at different times show that L-band is far superior to C-band in the vegetated areas, even when the observations are separated by only one day. These results imply longer wavelength instruments are more appropriate for studying surfaces by repeat-pass observations.

Introduction

SIR-C background

In April and again in October, 1994, the space shuttle Endeavor mapped the earth with the Space Radar Laboratory (SRL), comprised of Shuttle Imaging Radar-C (SIR-C), a dual frequency, four polarization radar instrument plus the single frequency and polarization X-SAR radar. The imaging radar suite measured the surface radar backscatter intensity and coherent backscatter phase at fine spatial resolution over the radar swath. Most of the radar investigations interpreted the multispectral, multi-polarization measurements provided by SRL to map biomass, soil moisture, terrain types and natural hazards. Many of these results are reported elsewhere in this issue.

The SIR-C spaceborne radar interferometry demonstration has literally added a new dimension to the more conventional imaging radar applications. In radar interferometry, multiple images of an area acquired on different orbits are combined coherently to obtain estimates of the surface topography and any change to the topography that occurred between the observations. Previous studies with airborne and spaceborne platforms have demonstrated the high level of precision and automation possible for topographic mapping applications afforded by interferometry (Zebker and Goldstein, 1986; Zebker *et al.*, 1992). Spaceborne radars on the ERS-1 and JERS-1 satellites have been used for surface deformation studies, including co-seismic deformation (Massonnet *et* al., 1993a; Zebker *et al.*, 1994 b), volcanic deflation (Massonnet *et al.*, 1994), and glacier motion (Goldstein *et* al., 1993) with millimeter scale precision.

Interferometry requires that the spatial orbital separation, or "baseline," between the two observations be small. This small baseline was achieved using two very different geometries. Six month temporal separation radar interferometry, which we emphasize in this report, was implemented by repeating some April orbit tracks during the October

mission. Interferometric data were also acquired with a one day repeat period during the second mission under similar orbital constraints. Six month interferometry has the potential for surface deformation measurements, while one day interferometry can be used for certain topographic mapping, coherence, and glacier motion studies.

Pre-flight uncertainty in orbit knowledge limited the scope of planned interferometry experiments. Mission planners adopted a conservative approach for orbit maintenance, aiming for zero baseline. In fact, during SRL-2 in October, shuttle engineers were very nearly able to reach their target, repeating orbits within a tube less than 200 m in radius. As a result, most of the interferometry orbit pairs form baselines too small for accurate topographic mapping, but well-suited to surface deformation studies. Table I summarizes the characteristics of the missions relevant to interferometry.

Two of the most rapidly deforming sites in the world were targeted for six month interferometry experiments: Kilauea, Hawaii and Long Valley, California. Rates from 2 to 10 centimeters per year have been measured at these sites, affording an opportunity to observe an interferometric signature through the noise. This paper describes the analysis of the Kilauea experiment. Figure 1 illustrates the imaging swaths at Kilauea in map projection.

Motivation I - GPS Measurements of deformation

The Kilauea volcano sits on the southeast flank of the island of Hawaii between Mauna Loa volcano and the sea. Kilauea has been active more or less continuously since 1983 with sporadic eruptions from the Pu'u O'o and Kupaianaha vents. Shallow magma reservoirs below the surface fill and empty over time, altering pressure on the surface, which then deforms. Lava tubes connecting subsurface chambers and the sea can open, causing eruptions from surface vents. Kilauea's motion is well monitored by a (mobile) GPS network. Deformation rates as high as 10 cm/year have been measured (see Fig.2), largely in the faulted basalts of the palis (the Hawaiian name for large fissures and fault

scarps) in the Southeast Rift Zone.

Kilauea serves as a good demonstration site because Kilauea's motions have been well mapped by GPS and the deformation rates are relatively high. Eruption prediction is not the primary motivation for studying the site, as geologists have had some success in anticipating eruptive events through high accuracy geodetic measurements, and by monitoring seismicity.

Motivation 11- Differential interferometry successes in the past

Differential interferometry, a technique by which surface deformation is measured, is a powerful method for obtaining the displacement in the direction of the radar line-of-sight with mm-scale precision; at m-scale resolution, and over km-scale areas. A variety of deformation signatures have been mapped by this method, including mm-scale ground motion in agricultural fields (Gabriel *et al.*, 1989), m-scale ice stream motion in Antarctica (Goldstein *et al.*, 1993), cm- to m-scale coseismic displacements (Massonnet *et* al., 1993; Zebker *et al.*, 1994; Peltzer *et d.,* 1994; Peltzer and Rosen, 1995; Massonnet *et aL,* 1995a), and possible cm-scale volcanic deflation (Massonnet *et al.*1995b). Detailed analysis of the deformation signatures of both the 1992 Landers earthquake (Peltzer *et* a}., 1994) and the 1993 M=6.1 Eureka Valley earthquake (Peltzer and Rosen, 1995) shows that, in addition to the overall consistency with standard geodetic measurements, the fine resolution and spatial coverage can provide insight into the slip mechanism that is unattainable from the seismic record, with or without a dense G PS network in place.

The SIR-C data are superior for interferometric studies in many respects to other synthetic aperture radar (SAR) data, especially over Kilauea. S1 R-C acquired imagery at two frequencies simultaneously, allowing direct observation of frequency-diverse scattering effects. Also the low orbital altitude and high transmit signal power give a very clean signal. ERS-1 data cannot presently be collected over Hawaii because it does not lie within range of an ERS ground receiving station. JERS-1 data is difficult to

acquire for interferometry applications, and orbits are difficult to predict. JERS also suffers from a high noise level. Thus the SIR-C experiments contain fundamental y new observations that expand understanding of the strengths and limitations of repeat-pass interferometry.

Observations and Data Reduction

Interferometer Equations

The theory of differential interferometry has been presented a number of times (e.g., Gabriel *et* al., 1989; Zebker *et* al., 1994), but certain relations are important to state here to support interpretation of the measurements.

The two imaging radars depicted in Fig. 3a separated by the "baseline vector" $\vec{B}$ are in motion perpendicular to the page, and represent the SRL platform nearly repeating its track. The phase at each point in a radar image is the sum of the backscatter phase ϕ_{bi} and the propagation phase $\phi_{pi} = -\frac{4\pi}{\lambda} r_i$, where r_i is the range from antenna i to the imaged point. For two radars imaging a scene at the same frequency and with similar viewing geometry, the backscatter phase will be nearly equal: $\phi_{b1} \approx \phi_{b2}$. Under these assumptions, the phase difference between the two images at a given point is

$$\Delta\phi = \phi_1 - \phi_2 = -\frac{4\pi}{\lambda}(r_1 - r_2) \tag{1}$$

For spaceborne geometries, where $|\vec{B}| << r$, we may write

$$\Delta\phi = -\frac{4\pi}{\lambda}\vec{B}\cdot\vec{l} = -\frac{4\pi}{\lambda}B\sin(\theta - \alpha) \tag{2}$$

where l is a unit vector in the look direction. In words, the phase difference is proportional to the component of $\vec{B}$ in the look direction, $B_{\parallel} = B\sin(\theta - \alpha)$. This is the parallel ray approximation used by Zebker and Goldstein (1986).

To see how this phase relates to topography, consider a surface devoid of local

topography. Then,

$$\Delta\phi_0 = -\frac{4\pi}{\lambda} B \sin(\theta_0 - \alpha) \tag{3}$$

where $t9_0$ is the look angle to a given pixel. If topography is present the look angle for a given range will be altered by $\delta\theta$ as illustrated in Fig. 3b:

$$\Delta\phi = -\frac{4\pi}{\lambda} B \sin(\theta_0 + \delta\theta + \alpha) \tag{4}$$

The "flattened" phase difference, formed by removing flat-earth phase

$$\Delta\phi_{\text{flat}} = \Delta\phi - \Delta\phi_0 \approx -\frac{4\pi}{\lambda} B \cos(\theta_0 - \alpha)\delta\theta \tag{5}$$

is to first order proportional to the perpendicular component of the baseline referenced to the flat earth, $B_{\perp 0}$ = B $\cos(\theta_0 - \alpha)$, and to the small angle $\delta\theta$, which in turn is proportional to the topographic height z: $\delta\theta \approx z/r_0 \sin 0_0$. The so-called ambiguity height is the elevation change required to alter the phase difference by one cycle (2π radians) and is given by

$$h_a = \frac{\lambda r_0 \sin\theta_0}{2B_{\perp 0}} \tag{6}$$

For the six-month repeat I,-band Kilauea observations, $h_a = 570m$.

The phase difference in repeat-pass observations measures ground motions in addition to topography. The range change in the second image A_T due to motion enters into the phase difference directly

$$\Delta\phi_{\text{flat}} = -\frac{4\pi}{\lambda} B \cos(\theta_0 - \alpha)\frac{z}{r_0 \text{SII}\theta\theta} + \frac{4\pi}{\lambda}\Delta r. \tag{7}$$

Note that the phase difference is far more sensitive to motions than to the topography itself. From Eq. 7, Ar = $\lambda/2$ gives one cycle of phase difference, while z must change by h_a to affect the same change.

Characteristics of the Inteferometric Phase

There are several fundamental problems in isolating the motion signature in an interferogram. The first is the occurrence of back scatter phase changes between

observations. These changes can lead to systematic biases to the phase difference measurements, and to randomization of the phase through signal decorrelation. Decorrelation can be a significant impediment to repeat-pass interferometric analysis. The measure of correlation is

$$\gamma = \frac{< c_1 c_2^* >}{\sqrt{< c_1 c_1^* >< c_2 c_2^* >}} \quad (8)$$

where c_1 and c_2 are the complex valued resolution elements of the two images that form the interferogram, * denotes complex conjugation, and <.> denotes statistical expectation, realized in practice by spatial averaging. There arc three major factors that contribute to decorrelation in repeat-pass interfer ometry: thermal noise, geometric decorrelation resulting from slightly different imaging, geometries and volumetric scattering, and temporal decorrel ation resulting from random wavelength-scale motion of scatterers within a resolution element (Zebker and Villasenor, 1992).

The second major problem in isolating motions from other phase modulations in an interferogram is the topography itself. Removing the topographic phase signature from an interferogram requires either a reference digital elevation model (DEM) of sufficient resolution and accuracy, or an independent interferogram with no motion present. Using a DEM, we may synthesize an interferogram if the imaging geometry is known. Subtracting the phase differences pixel by pixel removes the topographic phase and leaves only the phase clue to motion. For the six-month separation Kilauea observations, only two passes were available. Since no topography-only interferogram could be generated, the DEM method is used.

A third problem in isolating motions is the effect of the atmosphere on the radar signal. In observing the Earth, radar signals must propagate through the atmosphere, which induces additional phase shifts that are not accounted for in the geometrical model described above. There is extensive literature on this problem, mostly related to radar altimetry studies. We refer the reader to the review of Goldhirsh and Rowland

(1982) and references therein for more details.

Propagation through both the "dry" atmosphere and through atmospheric water vapor adds additional phase delays to the interferogram. In each case the amount of phase delay is inversely proportional to wavelength, that is, the medium is non-dispersive. Since the effect is evidenced as a nearly constant time delay of the radar signal, independent of frequency at microwave wavelengths, the contamination of the signal cannot be corrected using dual-frequency measurements, such as those commonly used in ionospheric corrections. Variability in the atmospheric medium on a time scale similar to the repeat orbit interval then represents an unpredictable error signal which adds to the desired phase signal.

Thus any interferometric technique will be compromised if propagation effects such as these variable time delays alter the observed phase significantly. In the case of surface deformation, the true motion of the ground between observations will be falsely indicated in the interferogram by an amount equal to the difference of the equivalent excess propagation length through the atmosphere on the two passes. In the case of topographic measurements, the distortion depends also on viewing geometry and baseline parameters, as reflected in the above Eq. 7 for topographic error.

The amount of delay that might be expected from atmospheric variability can be estimated from an equation used by the SEASAT radar altimeter science team to remove both the dry and wet tropospheric influences from that instrument's data. Their model, as quoted in Goldhirsh and Rowland (1982), is

$$Ax = 2.277 \times 10^{-3}\left(0.05 + \frac{1255}{T_s}\right)e_s + (2.277 \times 10^{-3} - 1.11 \times 10^{-5}\cos\Lambda)P_s \qquad (9)$$

where Ax is the nadir-looking excess path length through the atmosphere, P_s is the surface atmospheric pressure in millibars, T_s is the surface temperature in Kelvins, and e_s is the surface partial pressure of water vapor in millibars, and A is latitude. These constants are assumed valid to within about 0.5% for frequencies up to 30 GHz and

normal variations in pressure, temperature, and humidity.

If the nadir-looking path length is scaled by the obliquity factor due to our look direction, and multiplied by $4\pi/\lambda$ to get phase, we can estimate the phase signature of atmospheric variation. We find that a change in pressure from 1000 mb to 1025 mb, a reasonably large (and unlikely) pressure difference, yields a line of sight two-way range difference of 8 cm, corresponding to a phase change of 4 radians at L-band, at a temperature of 300 K and a latitude of 35°. Similarly, a columnar change in relative humidity of 10% induces a two-way range difference of 4.9 cm (2.5 radians at L-band) under the same conditions. Either of these effects could easily mask or mimic cm-level deformation or small topographic features. These values will be compared below to the Kilauea interferogram measurements.

Data Reduction

Interferograms and Correlation Maps

For the methods of synthetic aperture radar image and interferometric processing, the reader is referred to the literature (see for example Curlander and McDonnell, 1991; Zebker *et* al., 1994a). The SIR-C processing team at J PL provided raw L- and C-band SAR data. Data acquired on the April and October flights were processed directly to interferograms using the processing parameters listed in Table II. The pixel spacing in the interferogram is roughly 50 m in ground range and in azimuth after 72 total looks. All interferometric images discussed in this work were manipulated at this pixel spacing. Figures 4a and 4b show the L- and C-band interferograms. The interferograms have been "flattened" as described above (Eq. 5), so that the fringes are primarily due to topography.

The most striking feature of these interferograms is the poor visibility of the fringes at C-band over most areas and good visibility at L-band everywhere. One way to quantify the quality of the fringes is through the correlation maps in Fig. 5. Regions

with poor fringe quality in Figs. 4a and 4b correspond to regions of poor correlation in Figs. 5a and 5b. The loss of correlation, in turn, corresponds to presence of vegetation on the surface. Figure 5c depicts the presence of vegetation on Hawaii as measured by the Noramlized Difference Vegetation Index (NDV1), formed from a combination of red and near-infrared channels of SPOT multi-spectral data. The NDVI is more a measure of chlorophyll density than biomass, however in the tropical canopy of Hawaii, they are closely related. The color scale in Fig. 5c has been chosen to highlight the relationship between decreased correlation and increased vegetation index. Referring to Fig. 5, recent lava flows in areas of the Pu'u O'o, Kupaianaha, and Mauna Ulu vents are relatively devoid of vegetation. Similarly, the Kilauea crater and desert region to its southwest are barren from lava flows and acid rain formed from sulphorous gases vented from Kilauea. The Mauna Loa slope to the west shows evidence of recent flows and is also unvegetated. All these regions have high correlation at both C and L band. All other regions have varying degrees of vegetation cover, and the interferometric correlation is accordingly lower.

The correspondence between decorrelation and vegetation is not one-to-one. The Mauna Loa flows directed northeast toward the city of Hilo appear to be barren in the NDVI figure, but show decorrelation in the radar data. Similarly, the coastal agricultural regions west of Hilo have much greater variation in vegetation index than the correlation maps show. Some changes to the vegetation cover may have occurred between the times of the SPOT and SIR-C images, particularly in the cultivated areas. Changes to soil moisture and water present on lava between the April and October SIR-C acquisitions can also influence the correlation.

One conclusion is readily apparent from these data, and has been corroborated with dozens of scenes examined by the authors at other sites: repeat-pass correlation at C-band in vegetated areas is poor, even with only one day between images. It is often so poor that surface properties such as topography or surface deformation, are

impossible to discern. Despite the plethora of C-band radar data available from ERS-1 and 2 and the upcoming Radarsat instruments, large portions of the earth will continue to elude interferometric scrutiny. Early attempts at measuring volcanic deformation were carried out using ERS-1 data in Alaska (Zebker *et* at., 1994 b), highlighting the limitations of the technique. Changes in the surface properties of the volcanos from weather and vegetation led to decorrelation of the images and no detectable deformation signature. Not until SIR-C have the advantages of longer wavelengths been so clearly demonstrated. The L-band signal more easily penetrates the canopy and scatters off the trunks and branches, which move less between observations. As the fringes of Fig. 4b show, L-band is a far more robust wavelength for repeat-pass interferometry in vegetated areas.

Two-Pass Differential Interferornetry

Because SRL-1 and 2 made only two repeated ascending passes over Kilauea, it was necessary to remove the topographic contribution to the interferometric fringes by simulating an interferograrn with topographic fringes from a 30-m DEM grid consisting of four mosaicked USGS 7.5' quadrangles. Substantial errors exist in this DEM because it was made well before the last decade, when the area around Pu'u O'o has rapidly built up from erupting lava. Pu'u O'o vent itself has grown by roughly 100 meters. Fortunately another high precision DEM exists of the chain of craters, made by the TOPSAR topographic mapping system (Zebker *et* al., 1992) in 1993. The TOPSAR DEM was mosaicked into the USGS mosaic.

Appendix A describes the procedure for simulating the interferogram. Approximate initial knowledge of the interferometer baseline plus the use of many ground control points from the DEM permitted a solution for the interferometric baseline. The baseline vector is not well-constrained because of phase distortions in the ground control points, however the most relevant component, $B_\perp$, is well-constrained. See Appendix B for a

discussion.

The simulated topographic phase was removed from the interferogram before phase unwrapping (App. B). Additional smoothing of this differential interferogram to a resolution of 100 m reduced phase noise for the phase unwrapping procedure, particularly in the decorrelated vegetated areas.

Figure 6 shows the differential interferograms at C-band (6a) and L-band (6b). Figure 6c shows the difference in the C and L band phase after scaling the L-band phase by the ratio of the wavelengths. Colorless regions of radar backscatter correspond to areas where unwrapping was not possible due to excessive noise.

Interpretation

Figures 6a and 6b show strong differential" phase variations. Since topography has been removed, the variations here are related to surface deformation, or atmospheric or ionospheric propagation delays. From Eq. 7, a positive phase change (blue to red to yellow in the figures) corresponds to an increase in the range Δr. If the phase changes are due to deformation, then the area south of Kilauea crater and on the seaward side of Hilina Pali show motion away from the radar. The area north of Kilauea in the rain forest on the other hand shows motion toward the radar. If the phase changes are due to propagation effects, the observations imply that there was more delay in October than in April south of Kilauea and at the Pali, and vice-versa in the rain forest.

The scaled phase difference in Fig. 6c does not have topographic, deformation, or non-dispersive propagation delay contributions; all are inversely proportional to wavelength and cancel in the difference. The remaining phase signature is related to dispersive propagation or surface scattering effects. The low altitude of the shuttle's orbit would rule out ionospheric effects. The strongest effects appear to correspond with surface features, implying that these are probably related to moisture content, vegetation density, or roughness characteristics of the lavas. The phase in Fig. 6c is

scaled to match the C-band phase; it is small compared to the phase excursions in Fig. 6a. Several features in Fig. 6c correspond to local areas of partial decorrelation in Fig. 5b, notably in Kiluaea crater itself, and in the Mauna Ulu area.

GPS-Radar Comparison

The phase of the L-band interferogram in Fig. 6b has a roughly constant value along the coast. This would be correct if only topography affected the interferometric phase and the topographic phase had been completed removed by the simulation process. However, with surface deformation and other phase distortions present, a uniform coast line may not be correct. Inaccuracy in the estimated baseline can also introduce small quadratic distortions of low spatial frequency to the interferometer phase (Zebker *et al.*, 1994a). Secular deformation rates are available at numerous GPS sites in the active region (Owen *et* al., 1995). These rates converted to six-month displacements and projected into the radar line-of-site direction provide deformation ground control points for a final quadratic least squares adjustment of the phase field. Table III lists the GPS points used as control. The one-sigma uncertainties for the estimates are given in parentheses. The clustering of GPS points at Kilauea causes an otherwise unconstrained quadratic fit to distort the phase field away from the control points. To place the needed constraint, supplemental control points were peppered throughout geologically inactive areas, with displacements set to zero. The points were chosen where possible in unvegetated regions. This procedure has some risk, however it did not change the essential shape of the phase signature in the region of active deformation. In fact, conservatism in rejecting vegetated areas for control points may be responsible for the large residual phase along the northern coast.

Figure 7 depicts the L-band phase field after the least-squares adjustment as apparent surface displacement in units of cm. The radar swath has been mapped to UTM coordinates. Red (green) denotes motion away from (toward) the radar. Note also

of this work can be summarized as follows.

An area of several square kilometers surrounding the Pu'u O'o vent shows distinctive displacement away from the radar. Peak deformation was centered south of vent itself. If the deformation is assumed to be entirely vertical, the surface deflated by a net peak 14 cm over the six month interval. The signal is localized, distinctive in shape and unique to the six-month interferometric observations. It is very u nlikely that it can be attributed to atmosphere or outgassing.

No convincing agreement was found between the radar observations and the GPS measurements of secular motion at Kilauea. There are "hot spots" in the radar interferograms corresponding to those regions most rapidly deforming according to GPS. The sense of motion and the size of the inferred displacements also corresponds roughly with the GPS measurements. However, detailed analysis revealed that

1. peak-to-peak uncertainties in the phase measurements due to wet tropospheric delay anomalies or the presence of gas plumes are likely to be as large as the displacement signature and may have structure correlated with topography or surface features.

2. the radar line-of-sight displacement is comprised of horizontal and vertical displacement components. Because the GPS measurements are inaccurate in the vertical direction, it is difficult to compare the GPS and radar observations for such small motions. The large uncertainties in the GPS projected displacement do not allow a well-constrained least-squares fit. Ignoring the noisy vertical component of the GPS displacement artificially reduces the uncertainties, but does not improve agreement between radar and GPS observations.

3. GPS-derived displacement ground control points were too sparsely located and inaccurate in the vertical to correct for the quadratic phase distortions introduced by poor orbit knowledge. Residual distortion can account for some of the excess

a scale interpreting the phase as topographic residuals; a topographic map derived from these data would have systematic errors as large as 600 m because of the small baseline involved. Several features of the image are noteworthy. The locations of maximum displacement away from the radar tend to appear along the coast, with the exception of a local feature associated with the Pu'u O'o lava vent (see inset in Fig. 7) and the Ka'u desert southwest of Kilauea crater. Displacements at the coast southeast of Hilina Pali and at the Ka'u desert are consistent in sign with, but larger in magnitude than, the GPS secular rates predict (see Fig. 2). The displacements measured in the northern coast near Hilo are not consistent with the few GPS measurements in the region, which show little or no motion. Thus the data appear to show evidence of the surface deformation signal, and other intriguing local features such as Pu'u O'o, yet artifacts in the phase confuse the interpretation.

Figure 8 plots the adjusted radar line-of-sight displacements of Fig. 7 against the GPS data projected into the radar line-of-sight for two cases: (a) where the three-dimensional GPS vector is used in the projection, and (b) where the vertical component of the GPS vector is assumed zero. It is well known that the vertical component in GPS measurements is not nearly as well constrained as the horizontal components, consistent with Table III and Fig. 8. Most vertical estimates are consistent with zero within their error bars. While there is likely to be a non-zero vertical component to the displacement, inclusion of it in these comparisons would require additional modelling. For consistency in computing Fig. 8b, the least-squares adjustment to the radar line-of-sight displacements was carried out with vertical GPS ground control displacement set to zero.

In both cases, the statistical correlation between radar and G PS observations is below 0.6. In Fig. 8a, the error bars in the GPS data are simply too large to give confidence in a result. While the error bars on Fig. 8b are smaller, the scatter about the fitted line is still quite large and the slope is clearly not one; the displacement derived

by radar appears to be twice the GPS estimate.

Including the neglected vertical displacement term might improve the result. For the southeast-hanging face of the fault associated with Hilina PaIi, the vertical displacement of the land is clearly downward as the surface moves outward from magma pressure and gravity. Thus the vertical GPS component is likely to be positive in the direction away from the radar, increasing the GPS derived estimate of the projected displacement. For slip on a fault plane with 45° dip and strike normal to the radar look direction (roughly the configuration of the observations), the vertical and horizontal motions are roughly equal. Such a configuration could account for the factor of two discrepancy shown in Fig. 8b.

In addition to the poor GPS measurement of the vertical displacement, other unknowns erode confidence in this GPS-radar consistency argument. While the error bars on the radar data are empirically determined from spatial statistics around each measurement site, little is known about the stationarity of the phase over space. The fit to the spatially distributed GPS displacements anchors the phase field on a scale of tens of kilometers, however, kilometer scale distortions may exist from propagation effects. The magnitude of these distortions is poorly understood. An attempt to quantify these effects follows.

Figure 9 shows L- and C-band differential interferograms of an area near Kilauea volcano derived from data collected on Oct. 7 and 8, 1994. The topographic signature was removed using the two-pass approach, thus if the surface did not deform appreciably over the one-day period we would expect to observe uniform phase everywhere. Note that the variability in the C-band data tracks the L-band changes exactly save for i) a factor of about 4 (the wavelength ratio) and ii) regions of denser vegetation where the correlation at C-band was too low to permit accurate phase retrieval. Residual topography is negligible, as the one-day repeat baselines are very small (similar to the six-month repeat baseline). These variations are thus due to either surface movement or

to propagation through a neutral medium.

The measured rms phase residual in the image is 0.7 radians at L-band. This corresponds to an excess two-way path length of 2.6 cm. Peak-to-peak variations in the phase residual can reach as high as one cycle at L-band, particularly near the coast east of Pu'u O'o (not shown in the figure). Since it is highly unlikely that the surface is undergoing such large deformation in one day without notice by any other technique or individual, we must conclude that the distortions are due primarily to variations in the atmosphere, as no other source seems likely.

It is unlikely that large variations in atmospheric pressure from point to point in the image could occur under normal circumstances, and no anomalous weather conditions were reported for the time of the observations. Hence it is more probable that what is dominating the signature in Fig. 9 is natural variation in the distribution of water vapor and how that distribution changes from the time of the first observation to the time of the second. The six-month interferogram shown to the left in Fig. 9 also shows phase variations, but their spatial characteristics are quite different. The kilometer-scale random deviations attributed to water vapor in the one-day interferogram are largely absent in the six-month interferogram. In addition, the smoothly varying phase variations in the six-month pair can often be associated with surface features, whereas the one-day pair data does not show such structure. The only substantive difference between these interferograms is the acquisition time. The six-month pair was acquired at 2 AM local Hawaii time, while the one-day pair was acquired mid-day. The increased variability in the water vapor in the daytime points to solar-driven convection in the air mass above the island as a mechanism.

. It is tempting to infer from this comparison that water vapor does not corrupt the six-month measurements at a level sufficient to mask the deformation signal. However, little is known about the spatial distribution of water vapor. While the smaller scale variations of water vapor seem to disappear at night, the larger scale features, such as

accumulation along the coast or collocation with vegetation may remain. Though some of the six-month signal is most likely deformation, it is difficult to extract.

GPS-based Tropospheric Estimates

GPS based estimates of the wet tropospheric delay were examined to better understand the magnitude of the delays inferred from the differential interferograms. Estimates of the wet-zenith delay from GPS and VLBI data have been shown to compare favorably with those from water vapor radiometers (Yunck, 1995). GPS techniques involve modeling the wet-zenith delay as a random walk process that is allowed to vary 1 cm in 1 hour or 5 cm in 24 hours. Agreement with radiometer-derived estimates ranges from 3 to 12 mm and is typically less than 10 mm.

Several GPS receivers were operated on Kilauea by the Hawaiian Volcano Observatory of the USGS during the October shuttle over-flights. These stations collected data for up to three days. The altitudes of the stations range from near sea level to 3000 ft.

A useful measure of the tropospheric variability is the delay difference at a station from one day to the next, as shown in Fig. 10 for the KAEN station. These differences show peak-to-peak variability of 6 cm zenith delay, which maps to a two-way radar path delay exceeding 12 cm, commensurate with the peak-to-peak variability of the one-day measurements. Similarly, the rms deviations of the zenith delay is on the order of 1 cm, consistent with the rms spatial variability of the one-day radar measurements. This consistency depends on the ergodic assumption that the temporal variability of the wet troposphere seen in Fig. 10 is representative of a spatially fixed distribution that moves slowly with the wind,

Pu'u O'o deformation signal

Another possible explanation of the features emanating from Kilauea and hovering over Pu'u O'o is the presence of gas plumes. Water vapor and sulphur dioxide gas are frequently vented from Kilauea. Acid rain carried to the southwest by trade winds contributes to the desertification of the Southwest Rift Zone, notably Ka'u desert. The shape of the differential phase signature for Kilauea is particularly clear in Fig. 6, where the C-band phase is fan-shaped, with its tip emanating from the edge of the caldera toward the southwest. Pu'u O'o is also venting gas in this period of activity. Assuming that the atmosphere is at 50% relative humidity, that the plume is 100% water vapor, and that it has expanded to nearly the same temperature and pressure as the background atmosphere, the plume must displace only about 10% of the atmospheric column to yield a signal of 2.5 radians. Thus a plume present on one observation and not the other could also be responsible for some of the observed signals.

For the signature at these locations to be due to gas plumes, it must represent a difference in the atmospheric refractivity from April to October. Both signatures imply greater radar path length, suggesting that the outgassing activity was greater in October than April. Unfortunately, records of plume activity are not kept in the detail needed to corroborate these observations.

The shape of the phase signatures is quite different. If one assumes that the prevailing winds are similar at Kilauea and Pu'u O'o, then it is unlikely that both signatures are plumes: the Kilauea phase anomaly is elongated to the southwest, while the Pu'u O'o anomaly is centered over the vent. A plausible yet entirely uncorroborated explanation that is consistent with GPS measurements is as follows: The signature at Kilauea is not due to plume activity, but is actually the expected wide-area deformation signal. The signature at Pu'u O'o is either due to localized deflation of the magma reservoir beneath the vent, or it is due to a nearly vertical column of gas above Pu'u O'o.

Continuing this line of argument, it is possible to rule out gas venting at Pu'u O'o by comparing the six-month differential phase signature to several interferograms from the October one-day repeat observations, as shown in Fig. 11 Panel (a) shows the six-month L-band signature in radar coordinates. Panels (b-d) show the L-band signatures formed from l-day, 2-day and 3-day repeat periods. As noted above, for the signature in Panel (a) to result from venting, it must have occurred on October 4, 1994, when the second six-month repeat image was acquired. However, the differential interferograms in Panels (b-d) were formed from data acquired on four days after October 4, and these show no evidence of anomalous phase surrounding the Pu'u O'o vent. These observations imply that the signature is not related to propagation delays, but rather reflect deformation of the surface around the vent.

Careful examination of Panel (a) shows that the center of greatest deflation occurred to the south of the Pu'u O'o vent, peaking at roughly 8 cm of deflation in the radar line-of-sight. For purely vertical motion, this translates to roughly – 14 cm peak displacement. Ground observers saw no lava breakouts at Pu 'u O'o itself in the six month interval, and the radar observations are corr oboration. Resurfacing from lava would lead to complete decorrelation of the interferogram, as measured at numerous breakouts downslope in the area in the one-day repeat data (Zebker *et al.*, 1995). While some decorrelation is observed around Pu'u O'o itself, it is not severe enough to be caused by resurfacing. Deflation around the vent could occur as the magma reservoir beneath is depleted through the downslope breakouts. Again, there are no corroborating measurements with the required mm-level sensitivity at Pu 'u O'o itself.

Discussion and Conclusions

In addition to the specific results pertaining to Kilauea, this study of surface deformation using SIR-C repeat-pass interferometry reflects on the capabilities and limitations of radar for small scale geophysical signals in general. The main conclusions

delay observed along the coast in the north. The presence of residual distortions severely limits the interpretability of small deformation signals.

The limitations posed here are not necessarily globally applicable. The atmospheric effects at Kilauea are generally an order of magnitude more severe than at non-tropical sites (see e.g. Goldstein, 1995), so these results may be viewed as a worst case. Nonetheless, it is appropriate to characterize the behavior of the effects on a more theoretical basis, and to explore strategies for reducing them. This is an area of active research. The empirical observations of delay in the one-day repeat interferograms form a useful data set for comparison with theory. No other active volcanoes were observed by SIR-C during the six-month interferometry observations, however continuing reduction of ERS and especially the longer wavelength JERS-1 radar observations of volcanoes are warranted by these results.

Plume activity is yet another hazard associated with volcanoes that requires monitoring, particularly for aircraft safety. The all-weather, day-night capability of radar and its fine phase sensitivity to measuring refractive change could provide a substantial new capability in hazard assessment. The simple calculations presented here of refractivity changes due to plume activity at volcanoes, coupled with the observation of a phase signature that looks like a wind-blown plume trail at K ilauea, points to a new area of investigation for interferometry. Again, study of other volcanoes with active vents using ERS or JERS data is needed to better characterize these effects.

One of the more important lessons of SIR-C repeat-pass interferometry is the limitation imposed on topographic accuracy. Atmospheric effects can unacceptably distort the phase, resulting in large height errors, especially for short baseline observations. Care must be exercised in designing a repeat-pass topography mission to trade off the long baseline necessary for minimizing these distortions, and the short baseline required for reliable processing over a wide range of incidence angles. Furthermore, for both topography and topographic change, it is clear that decorrelation

due to vegetation severely limits the usefulness of short-wavelength (C-band or shorter) radars in repeat-pass interferometry.

Appendix A – Interferogram Simulation Method

Simulation of a radar interferogram requires spacecraft ephemeris information, a DEM of the region of interest, and radar operating parameters, The simulation proceeds by generating a synthetic image and height map in radar imaging coordinates. This two-dimensional coordinate system has one dimension as the distance, or "range," from the antenna to a specified point on the ground when that point was imaged by the radar, and the other dimension as the distance along track, or "azimuth," from some reference position on the orbit track when the point was imaged. Thus the radar imaging coordinates are easily computed using simple geometry given the position of the platform when a point in the DEM was imaged.

The platform position at the time a particular point is imaged is a function of the processing algorithm used to generate the SAR image. The algorithm can be made to synthesize a radar looking arbitrarily forward or backward along the orbit track direction. For Kilauea observations, the radar antenna boresight was nearly orthogonal to the direction of shuttle motion, so the data were processed to fix the sythetic boresight in precisely the orthogonal direction.

For each DEM coordinate, the position along the orbit track where the radar imaged that point is' determined by searching' iteratively through the reconstructed state vectors of the shuttle's orbit for the intersection of the plane normal to the flight direction and the DEM point. Once this position is determined, simple vector geometry allows the computation of the range from the antenna to the DEM coordinate. The height at that coordinate is then transcribed into a two-dimensional array indexed by range and along-track position.

After all DEM coordinates are mapped, the resulting "range-azimuth" image may be sparsely filled; the mapping from map coordinates to slant range coordinates is not regular when topography is present. The vacant image points are typically few, and are filled in by interpolation.

Theshuttle ephemeris vectors were specified relative to the WGS-84 datum and the DEM points in UTM coordinates of the Old Hawaiian Datum. Conversion from the northing-easting values of the Old Hawaiian UTM datum to latitude and longitude followed Snyder, 1982. Conversion from latitude, λ, longitude, θ, and height above the WGS84 ellipsoid, h, to rectangular coordinates (X, Y, Z) used

$$X = (r_e(\lambda) + h)\cos(\lambda)\cos(\theta) \tag{10}$$

$$Y = (r_e(\lambda) + h)\cos(\lambda)\sin(\theta) \tag{11}$$

$$Z = (r_e(1 - e^2) + h)\sin(\lambda) \tag{12}$$

(13)

where $r_e(\lambda)$ is the radius of curvature in the east direction given by

$$r_e(\lambda) = \frac{a}{\sqrt{1 - e^2 \sin^2(\lambda)}}, \tag{14}$$

e^2 is the square of the eccentricity of the figure of the earth, and a is the semi-major axis. WGS-84 vectors are obtained to within 5 m accuracy by adding an offset vector to the rectangular coordinates obtained above. WGS84 and Old Hawaiian datum parameters and the datum offset values are given in Table IV. Failure to convert from UTM to rectangular coordinates properly results in distortions such a skew and higher order warping that inhibit the fine co-registration between the simulated and measured interferogram required for differential interferometry applications.

In addition to the height, the radar brightness is simulated. Radar brightness is proportional to the local incidence angle according to the surface's backscattering phase function. The local incidence angle is determined from the local slope (the numerical gradient of the DEM) and radar line of sight vector. A very realistic brightness image arises from assuming a $\cos^n()$ phase function.

The orbit is not known precisely, so the simulated imagery does not align perfectly with the radar image. A straightforward brightness correlation gives the offsets required

to register the simulation to the data.

Appendix B – Baseline Estimation

With the unwrapped interferogram phase and the topographic heights available in the same slant-range coordinate system, a precision baseline can be estimated from thousands of "ground control points" through Eq. 2. The phase computed from the interferogram is known only modulo 2π radians, whereas the phase field representing the topography and surface change is a continuous field. It is necessary to unwrap the phase in a way that does not introduce error or phase inconsistencies (Goldstein *et al.*, 1988). Phase unwrapping errors are difficult to characterize, however they generally arise when the interferometric fringe rate is high or the data are very noisy. For the purposes of phase unwrapping, the interferogram was smoothed to a pixel resolution of 200 meters to reduce phase noise. The fringe rate at L-band is quite slow, so rapid fringe variation was not a significant problem.

The accuracy of the baseline is determined by the accuracy of the unwrapped phase and the DEM heights. The stability of the baseline estimate depends largely on the extent to which the measured image phase is related to topography. From Eq. 7, if the unwrapped phase has a component unrelated to topography of magnitude 2π radians, then the inferred topography will be in error by the ambiguity height, roughly 570 m. Such inconsistency will cause the baseline to be highly dependent on the "ground control points" used to derive it.

Two sets of control points were selected to determine the baseline: points covering the entire imaged area and points covering only the area north of the active deformation measured by GPS. The two baselines were quite different in length, however their perpendicular components were roughly the same (see Table V), This is understood from Eq. 7, which shows that the topography is determined to first order by $B_\perp$. The

second order term neglected in this equation contains the parallel baseline component:

$$\phi_2 = \frac{4\pi}{2\lambda} B_{\|0} \left(\frac{z}{\rho_0 \sin\theta_0}\right)^2, \tag{15}$$

This term varies by less than 0.1 radians over the extent of the scene's topography. The maximum topographic error induced by neglecting this term is 0.1 $h_a/2\pi \approx 10$ m, which is less than the accuracy of the USGS DEM. This implies that it is not important to know $B_{\|0}$.

This is fortunate, because phase distortions exceeding about 2 radians exist in the data and primarily influence the estimate of the parallel component. At the 200 m resolution of these unwrapped phases, the statistical phase noise is negligible. However, there is deformation of the surface present in the interferogram: GPS has measured a maximum rate of surface deformation of 5 cm in six months. From Eq. 7, this would correspond to about 2.6 radians of phase change at L-band. Other phase distortions, for example from propagation delays in the variable atmosphere, may also exist.

Acknowledgments. We are grateful to, SIR-C project for suggesting the six month observations of Kilauea, and providing the data expeditiously. Paul Segall gave us the benefit of his experience in GPS measurement in Hawaii and geophysical modeling. Scientists at the Hawaii Volcano Observatory described the nature of their *in situ* measurements at Kilauea. Robert Crippen of JPL kindly provided a mosaic of the USGS digital elevation model of Hawaii. This work was supported by the SIR-C Project under contract with NASA.

TABLE I

SIR-C RADAR SYSTEM PARAMETERS FOR KILAUEA OBSERVATIONS

Radar parameter	L-band	C-band
Frequency	1.240 GHz	5.285 GHz
Range bandwidth	20 MHz	20 MHz
Peak transmit power	6000 W	3000 W
System noise temperature	1100 K	1300 K
Pulse repetition rate	1250-1850	1250-1850
Antenna dimensions	12 by 2.9 m	12 by 0.7 m
Antenna elevation beamwidth	5“	5°
Critical baseline length	4000 m	935 m
Satellite altitude	215 km	215 km
Look angle	55°	55°
Ground range swath[2]	42 km	42 km

[1] 40 MHz for one-day repeat orbit observations

[2] 21 km for’ one-day repeat orbit observations

TABLE II

INTERFEROMETRIC PROCESSING PARAMETERS

Radar altitude	217820 m
Near slant range	387880 m
Processed range resolution	6.66 m
Processed azimuth resolution	6 m
Doppler centroid	O Hz
Interferogram range looks	6
Interferogram azimuth looks	12

TABLE III

GPS CONTROL POINTS FOR LEAST SQUARE ADJUSTMENT OF PHASE FIELD†

UTM Location		Displacement Vector			Radar Line-of-sight Displacement	
Lat.	Len.	North	East	up	Full vector[a]	No vertical[b]
(°)	(°)	(cm)	(cm)	(cm)	(cm)	(cm)
19.58892	-155.16576	0.57 (0.38)	0.27 (0.20)	-0.2 (1.9)	0.19 (0.79)	0.14 (0.18)
19.52525	-155.02570	-0.22 (0.74)	1.16 (0.35)	3.2 (2.9)	-1.15 (1.06)	-0.36 (0.37)
19.46511	-155.16674	0.29 (0.47)	1.10 (0.25)	-0.7 (2.2)	0.01 (0.88)	-0.16 (0.22)
19.45806	-155.11532	-0.19 (0.52)	1.10 (0.30)	0,2 (2.4)	-0.38 (0.96)	-0.33 (0.23)
19.42111	-155.28680	0.24 (0.41)	-0.56 (0.22)	-7.4 (2.3)	2.10 (0.98)	0.22 (0.19)
19.40259	-155.06557	2.36 (0.42)	-0.23 (0.22)	3.9 (2.1)	-0.03 (0.82)	0.91 (0.20)
19.39293	-155.29144	4.78 (0.67)	-3.79 (0.42)	-5.5 (4.8)	4.01 (2.15)	2.62 (0.28)
19.37333	-155.45803	2.55 (0.81)	-0.30 (0.37)	-3.1 (5.2)	1.78 (2.32)	0.98 (0.40)
19.37149	-155.20542	-0.53 (0.49)	-0.61 (0.26)	-9.3 (2.7)	2.26 (1.11)	-0.04 (0.23)
19.36821	-155.42064	-0.88 (0.82)	-0.43 (0.41)	4.8 (7.6)	-1.45 (3.54)	-0.21 (0.39)
19.35539	-155.32242	5.08(0.61)	-2.08(0.31)	-8.5(4.0)	4.47(1.74)	2.32 (0.29)
19.35053	-155.25422	4.68 (0.52)	-4.38(0.26)	-1.8(2.3)	3.19(0.90)	2.74 (0.25)
19.32647	-155.22809	1.44 (0.85)	-5.83(0.41)	-3.2 (3.8)	2.72(1.47)	1.93 (0.42)
19.30098	-155.37127	2.52 (0.67)	-0.32(0.34)	-0.6(5.4)	1.13(2.43)	0.98 (0.32)
19.29451	-155.30732	2.11 (0.44)	-2.98(0.23)	0.9(2.0)	1.25 (0.80)	1.47 (0.21)
19.27570	-155.25958	2.55(1.24)	-5.50(0.43)	-7.8(5.6)	4.18(2.09)	2.25 (0.69)
19.25985	-155.19265	4.26(0.85)	-7.64(0.40)	4.1 (4.1)	2.40 (1.58)	3.40 (0.42)
19.23781	-155.44720	1.50(0.63)	-0.15(0.39)	2.0(7.6)	0.06(3.63)	0.57 (0.26)

† GPS vectors courtesy of HVO. Yearly rates divided by 2 to obtain 6-month displacements.

[a] Projection of the three-component GPS displacement vector into the radar line-of-sight direction

[b] Projection into radar direction assuming the vertical component of GPS displacement vector is zero

TABLE IV

COORDINATE REFERENCE SYSTEM DEFINITIONS

Parameter	Value	
	WGS-84	Old Hawaiian Datum
Semi-major axis	6378137.0	6378206.4
Square of eccentricity	0.00669437999015	0.0067686579
DX	–	61
DY	–	-285
DZ	–	-181

TABLE V

BASELINE ESTIMATES

	Entire Image	North Image
$\|B\|$ (m)	143.8	103,0
α (^{0})	176.0	-172.0
B_c (m)	-143.4	-102.0
B_h (m)	10.1	-14.4
$B_\perp$ (m)"	-68.0	-66.7
$B_\parallel$ (m)	[a] -126.6	-78.5

[a] Computed for $\theta = 57.6°$

Figure 1. SIR-C Imaging geometry of Kilauea, Hawaii. At 14:20 GMT on April 13, and October 4, 1994, SIR-C mapped the 50 km swath shaded in gray for six-month surface deformation studies using radar interferometry. At 21:40 GMT on October 7, 8, 9, and 10, 1994, SIR-C mapped the 25 km crossing swath for studies of active lava flows. The abbreviation "Ku." marks the Kupaianaha vent.

Figure 2. GPS measurements of surface deformation (from owen *et al.*, 1995; Copyright 1995, Science). The secular rate of deformation is as high as 10 cm/yr near Hilina Pali.

Figure 3. Interferometric geometry. (a) Two apertures separated by a baseline $\vec{B}$ are flying into the paper imaging a swath on the ground. For SIR-C, apertures represent a single antenna nearly repeating its orbit track. (b) Conventions in linearizing the interferometer equations.

Figure 4. SIR-C Interferograms of Kilauea, Hawaii at (a) C-band, and (b) L-band formed from April and October images. One cycle of interferometric phase change, or "fringe," is coded as one excursion around the color wheel. Color is modulated in brightness by the magnitude of the mean cross correlation of the images $|< c_1 c_2^* >|$. Bright areas have high correlation and good fringe quality. Dim areas have poor correlation and fringe quality. One L-band (C-band) fringe corresponds to 570 m (135 m) of topographic variation.

Figure 5. SIR-C Correlation Maps of Kilauea, Hawaii at (a) C-band, and (b) L-band. (c) NDVI vegetation measure mapped to radar coordinates. Areas of poor correlation generally correspond to areas of high vegetation. C-band interferograms decorrelate much more severely due to vegetation than L-band data.

Figure 6. Differential Interferograms at (a) C-band, (b) L-band, and (c) scaled difference $\Delta\phi_C - (\lambda_L/\lambda_C)\Delta\phi_L$. Gray areas correspond to areas where correlation was too poor to give reliable phase estimates. Areas of phase change in the scaled difference often show decreased correlation in Fig. 5, suggesting a subtle rearrangement of surface scatterers from April to October.

Figure 7. Apparent surface displacement at L-band in map coordinates. Color scale represents one cycle of interferometric phase and can be interpreted as $\sim$ 12 cm peak-to-peak displacement of the surface along the radar line-of-sight direction, or residual topography of 570 m, peak-to-peak. Red corresponds to motion away from the radar, blue to no motion, and green to motion toward the radar. Signatures southwest of Kilauea caldera and at Pu'u O'o appear to be associated with surface features, independent of topography.

Figure 8. Comparison of radar line-of-sight apparent displacement to GPS displacements projected into the radar line-of-sight direction. (a) Using full GPS vector. (b) Assuming height component of GPS vector is O. 1)ashed line in (a) has slope equal to 1, but is not a fit to the data. Solid line in (b) is a fit to the data.

Figure 9. L- and C-band differential interferograms (at right) for one-day repeat orbits, October 7 and 8, 1994, compared to L-band six-month interferogram (at left). Six-month interferogram phase was anchored to GPS ground control points. C-band interferogram suffers from tropospheric effects, as well as severe decorrelation even at a one-day observation separation. Phase variance is larger in the one-day observations, and scale size of tropospheric effects differs from six-month data.

Figure 10. GPS estimate of wet tropospheric delay differences between days at a fixed GPS station. Peak-to-peak variation is 6 cm and an rms value is 1 cm. Night-time values are unknown, but are likely to be comparable in magnitude, if not in spatial structure.

Figure 11. Comparison of Pu'u O'o phase signature at L-band in six-month (top image and graph) and one-day (lower images and graphs) differential interferograms. Computed standard deviation of each one-day phase profile is σ = 0.42 radians. A six-month profile parallel to the displayed cut but south of the active area has σ = 0.29 radians. The right-hand scale of graphs is downward displacement in the radar line-of-sight direction. Vertical displacement is obtained by scaling by 1 / cos θ_0 where the θ_0 is the incidence angle.

References

Curlander, J. C. and R. N. McDonough (1991). *Synthetic Aperture Radar Systems* and *Signs/ Processing,* Wiley-Interscience.

Gabriel, A. G., R. M. Goldstein, and H. A. Zebker (1989). Mapping small elevation changes over large areas: Differential radar interferometry. *J. Geophys. Res.,* 94, 9183-9191.

Goldhirsh, J., and J. R. Rowland (1982). A tutorial assessment of atmospheric height uncertainties for high-precision satellite altimeter missions to monitor ocean currents. *IEEE Geosci. Rem. Sens.* 20, 418-434.

Goldstein, R. M., H. A. Zebker, C. L. Werner (1988). Satellite radar interferometry: Two-dimensional Phase Unwrapping. *Radio* Science 23, 713-720.

Goldstein, R. M., H. Engelhardt, B. Kamb, and R. M. Frolich 1993. Satellite radar interferometry for montoring ice sheet motion: Application to an antarctic ice stream. Science 262, 1525-1530.

Goldstein, R. M. (1995). Atmospheric limitations to repeat-track radar interferometry, *Geophys. Res. Lett., 22,* 2517-2520.

Massonnet, D., M. Rossi, C. Carmona, F. Adragna, G. Peltzer, K. Fiegl, and T. Rabaute (1993). The displacement field of the Landers earthquake mapped by radar interferometry. *Nature, 364, 138-142.*

Massonnet, D. and K. Fiegl (1995a). Satellite radar interferometric map of the coseismic deformation field of the M=6.1 Eureka Valley, CA earthqauke of May 17, 1993. *Geophys. Res. Lett., 22, 1541-1544.*

Massonnet, D., P. Briole, and A. Arnaud (1995b). Deflation of Mount Etna monitored by spaceborne radar interferometry. *Nature, 375, 567-570.*

Owen, S., P. Segall, J. Freymueller, A. Miklius, R. Denlinger *et al.* (1995). Rapid deformation of the south flank of Kilauea volcano, Hawaii. Science, 267, 1328-1332.

Peltzer, G., K. Hudnut, and K. Fiegl (1994). Analysis of coseismic surface displacement gradients using radar ingerferometry: new insights into the Landers earthquake. *J. Geophys. Res.*, 99, 21971-21981.

Peltzer, G. and P. Rosen (1995). Surface displacement of the 17 May 1993 Eureka Valley, California, earthquake observed by SAR interferometry. Science, 268, 1333-1336.

Yunck, T. P. (1995). Coping with the atmosphere and icmosphere in precise satellite and ground positioning, Environmental effects on Spacecraft Positioning and Trajectories, *Geophysical Monograph 73, IUGG 13,* 1-16.

Zebker H. A., and J. Villasenor (1992). Decorrelation in interferometric radar echoes. *IEEE Trans. Geosci. Rem. Sens., 30, 950-959.*

Zebker H. A., and R. M. Goldstein (1986). Topographic mapping from interferometric SAR observations. *J. Geophys. Res.,* 91, 4993-4999.

Zebker H. A., S. N. Madsen, J. Martin, K. B. Wheeler, T. Miller, Y. Lou, G. Alberti, S. Vetrella, and A. Cucci (1992). The TOPSAR interferometric radar topographic mapping instrument. *IEEE Trans. Geosci. Rem. Sens., 30, 933-940.*

Zebker H. A., C. L. Werner, P. A. Rosen, and S. Hensley (1994a). Accuracy of topographic maps derived from ERS-1 inter ferometric radar. *IEEE Trans. Geosci. Rem. Sens., 32, 823-836.*

Zebker H. A., P. A. Rosen, R. M. Goldstein, A. Gabriel, and C. L. Werner (1994b). On the derivation of coseismic displacement fields using differential radar interferometry: The Landers earthquake. *J. Geophys. Res.,* 99, 19617-19634.

This manuscript was prepared with the AGU LaTeX macros v3.1.

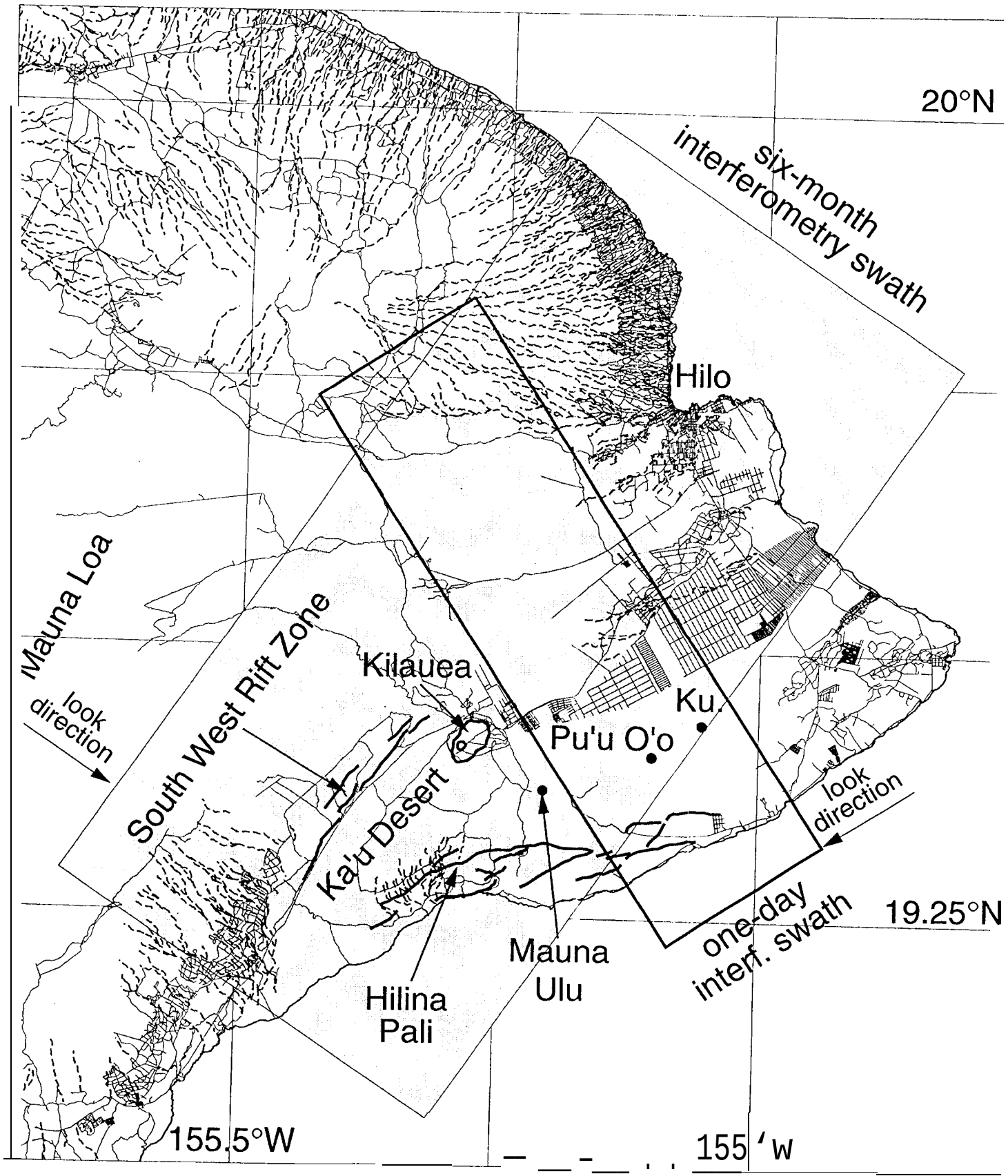

Figure 1 **Rosen** *et al.*
Surface deformation and coherence measurements of Kilauea Volcano, Hawaii from SIR-C radar interferometry

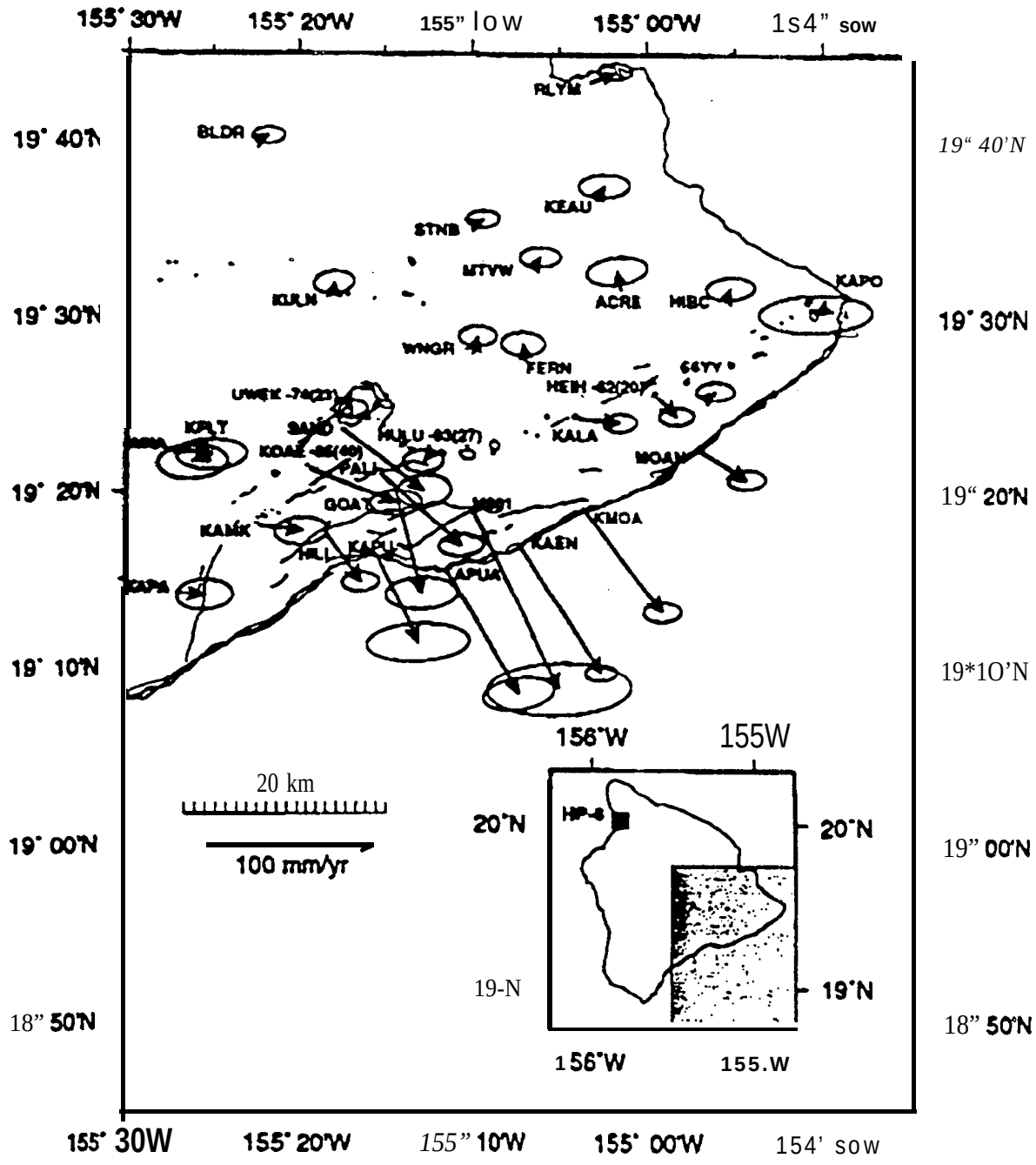

Figure 2 **Rosen** *et al.*
Surface **deformation and coherence measurements of Kilauea Volcano, Hawaii from SIR-C radar** interferometry

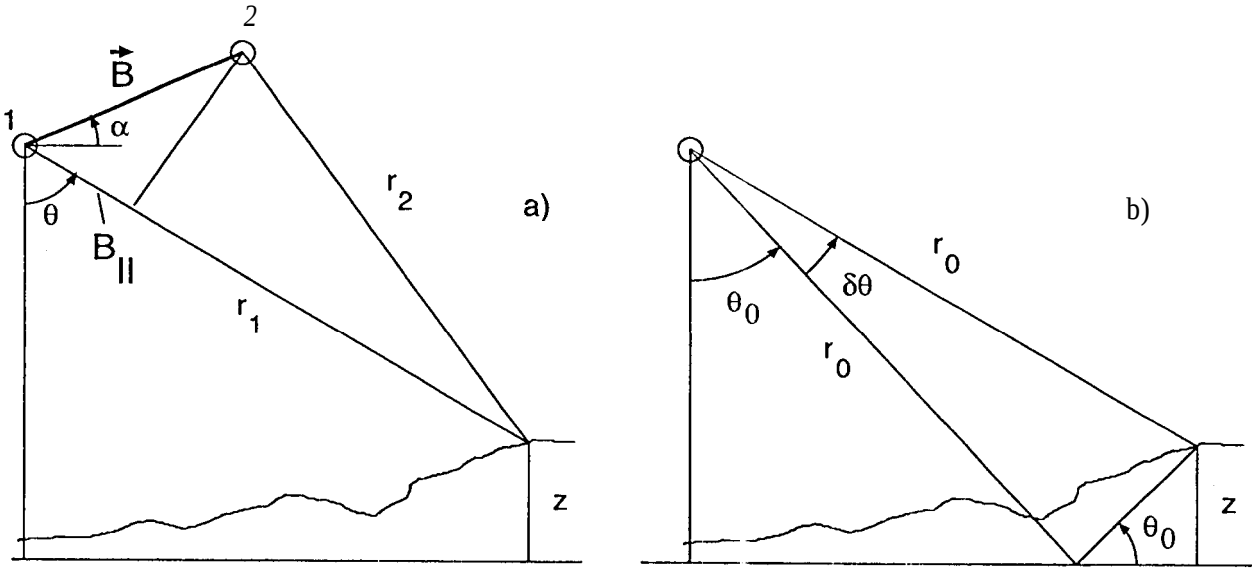

Figure 3 **Rosen** *et al.*

Surface deformation and coherence measurements of Kilauea Volcano, Hawaii from SIR-C radar interferometry

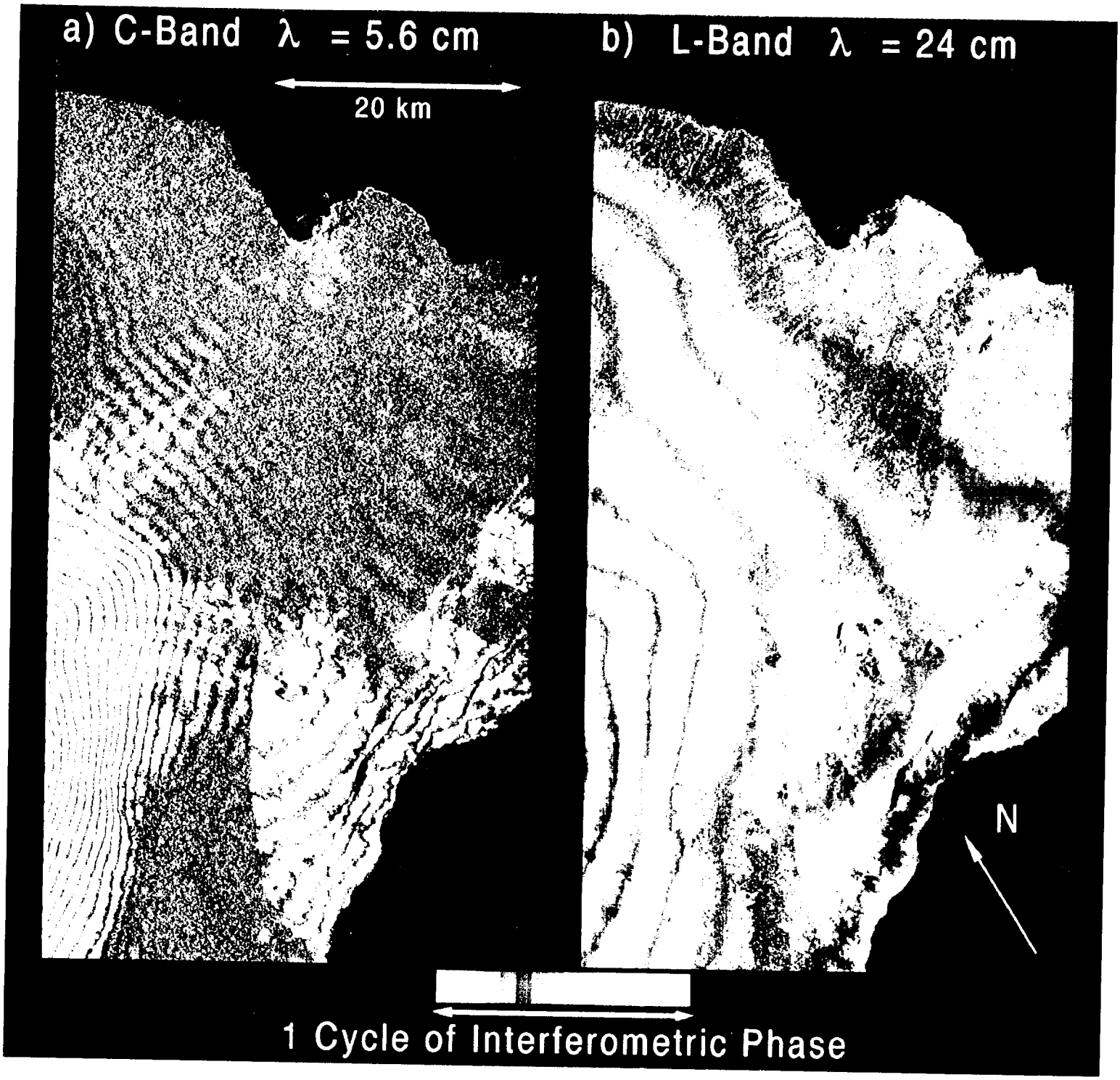

Figure 4 **Rosen** *et al.*

Surface deformation and coherence measurements of Kilauea **Volcano, Hawaii from SIR-C radar** interferometry

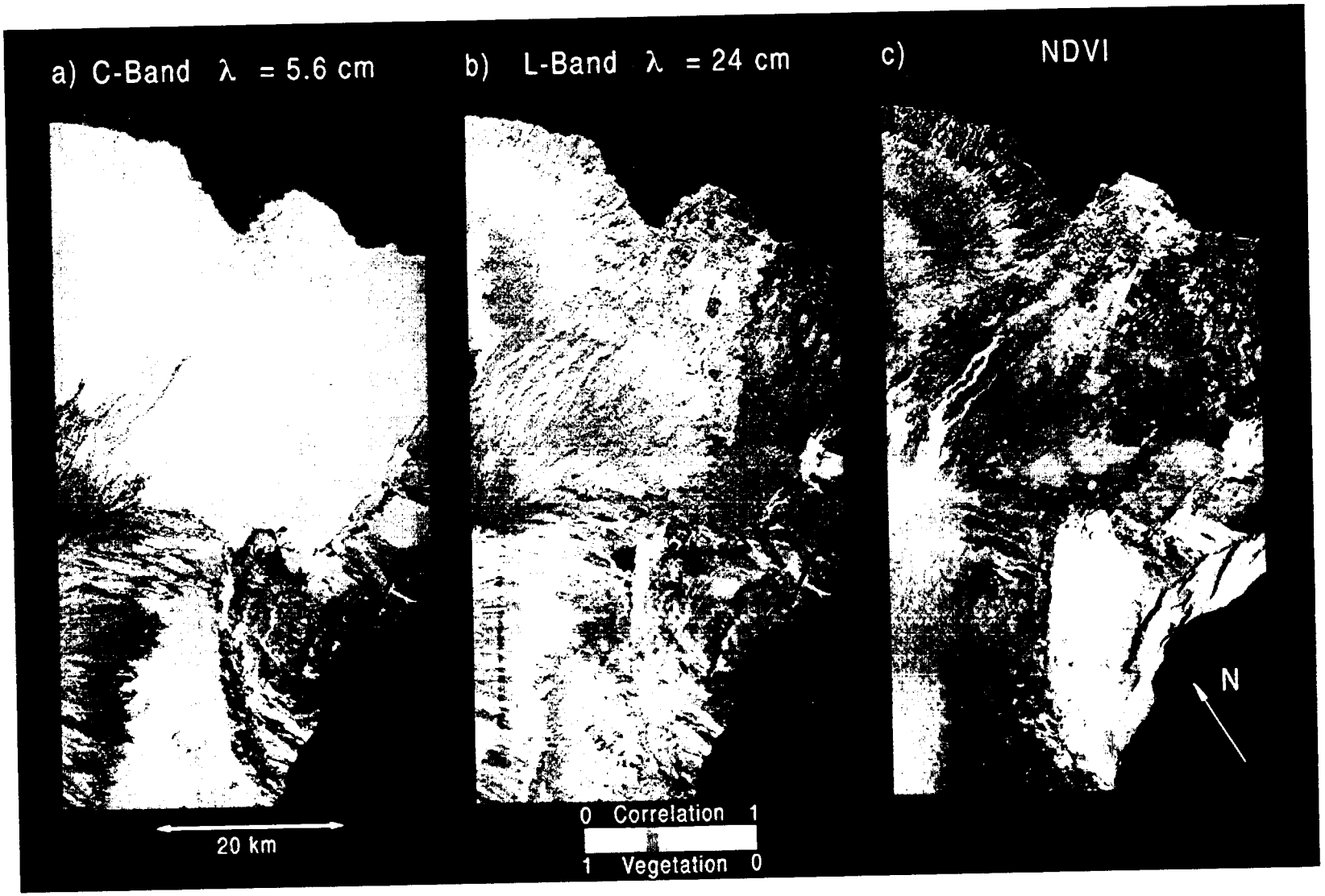

Figure 5 **Rosen** *et al.*

Surface deformation and coherence measurements of Kilauea Volcano, Hawaii from SIR-C radar interferometry

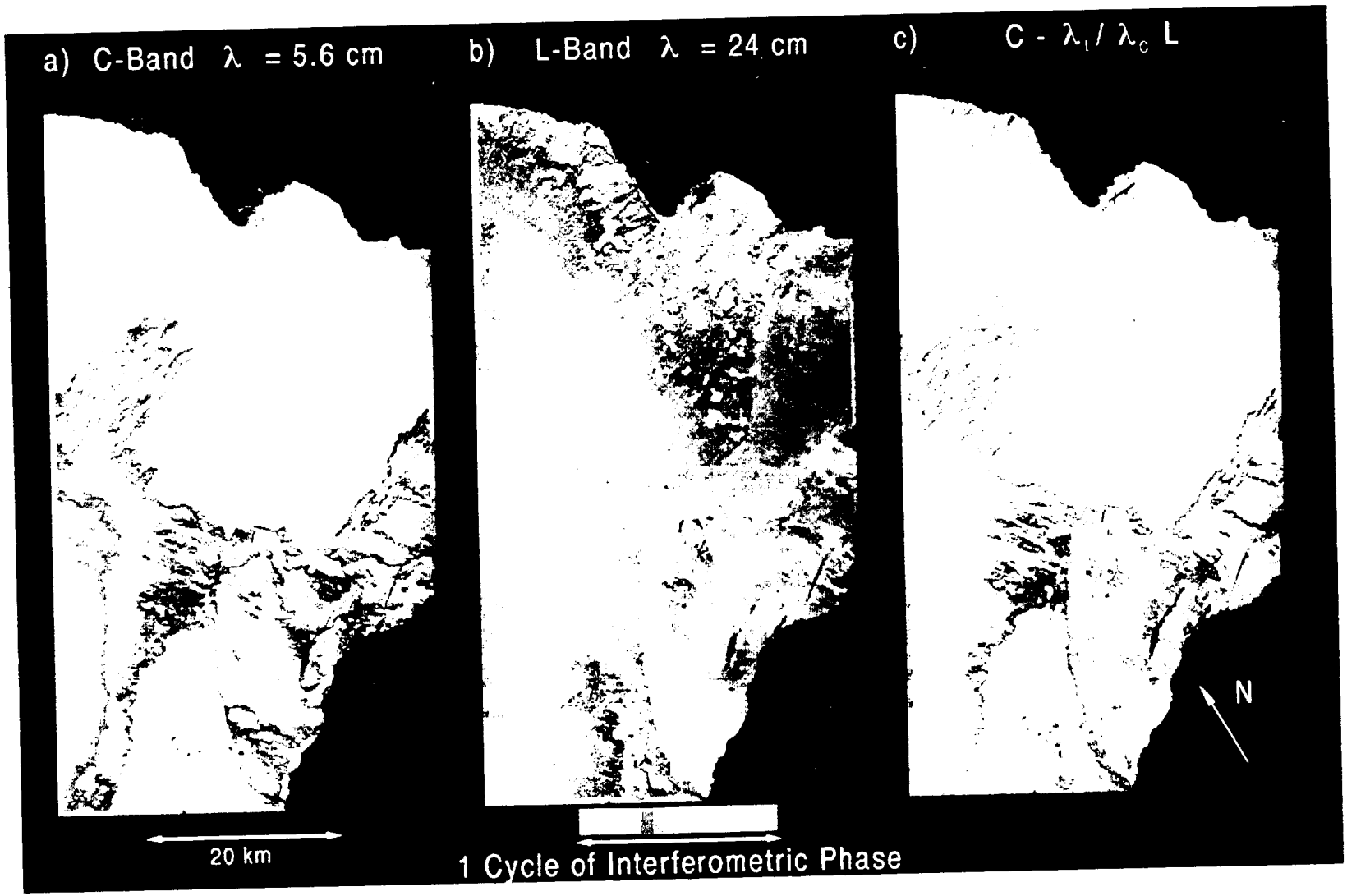

Figure 6 Rosen et *al.*

Surface deformation and coherence measurements of Kilauea Volcano, Hawaii from SIR-C radar interferometry

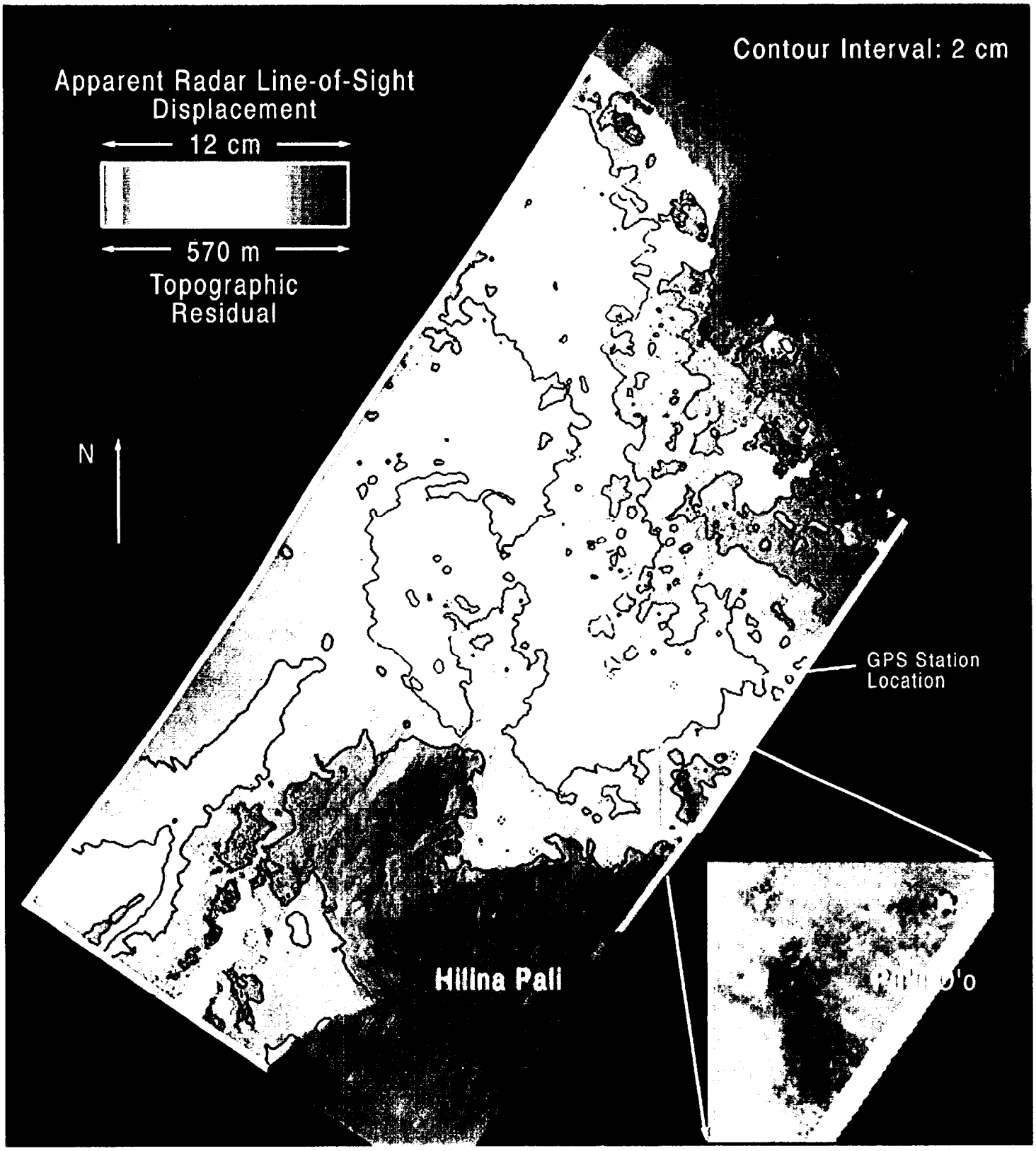

Figure 7 **Rosen** *et al.*

Surface deformation and coherence measurements of Kilauea **Volcano, Hawaii** *from* **JR-C** *radar interferometry*

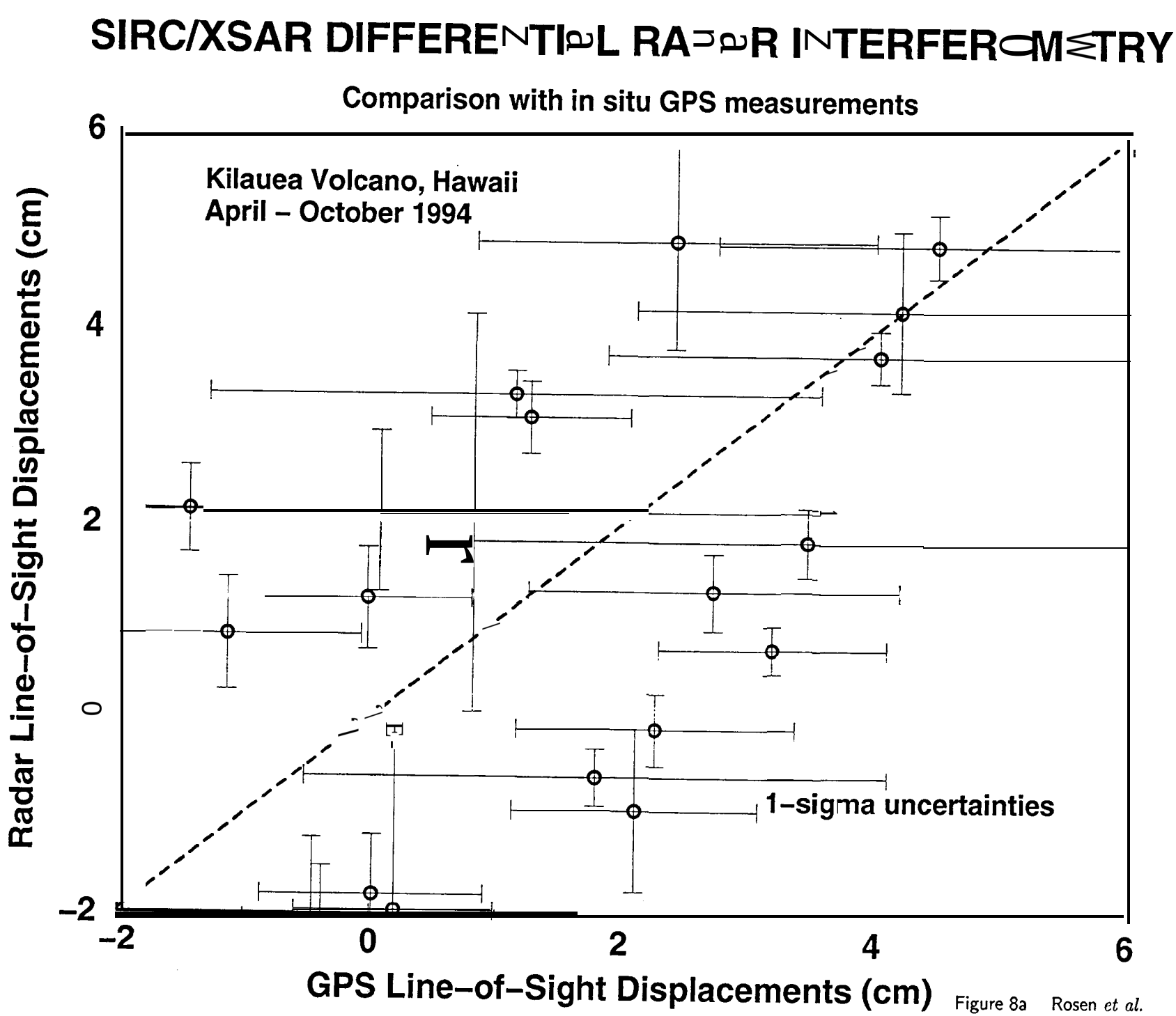

Figure 8a Rosen *et al.*
Surface deformation and coherence measurements of Kilauea Volcano, Hawaii

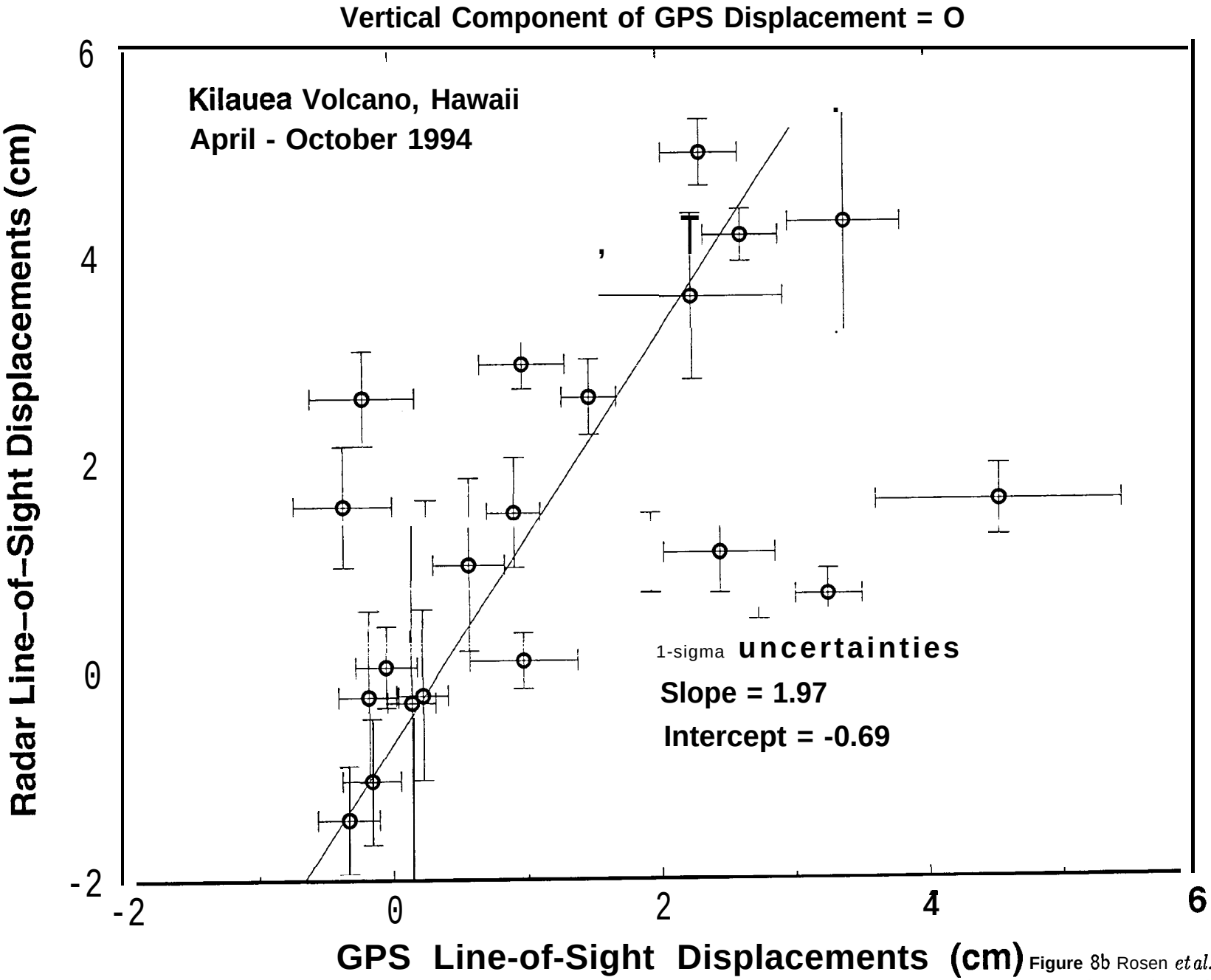

Figure 8b Rosen *et al.*
Surface deformation and coherence measurements of Kilauea **Volcano, Hawaii**

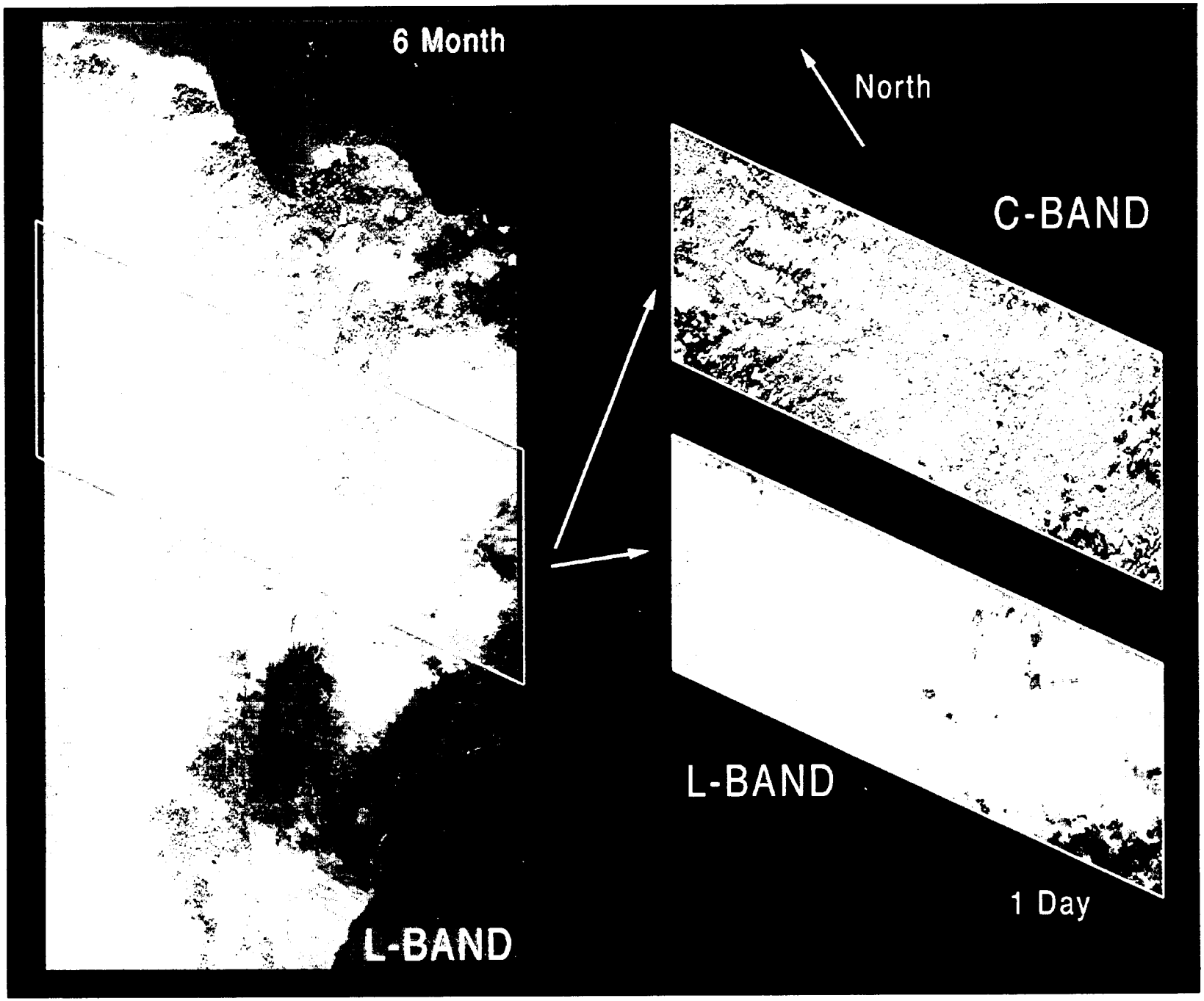

Figure 9 Rosen *et al.*

Surface deformation and coherence measurements of Kilauea Volcano, Hawaii

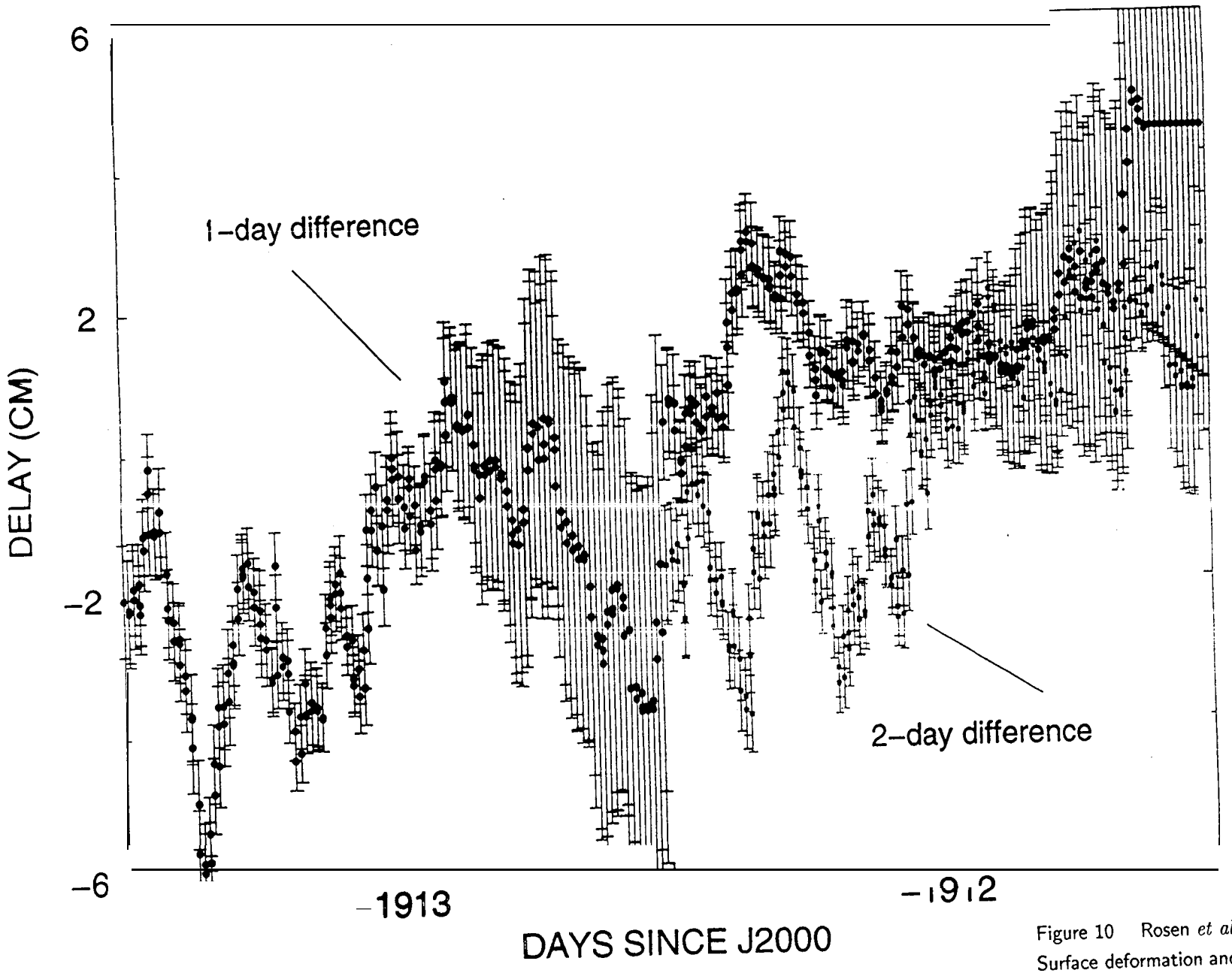

Figure 10 Rosen *et al.*
Surface deformation and coherence measurements of Kilauea Volcano, Hawaii from SIR-C radar interferometry

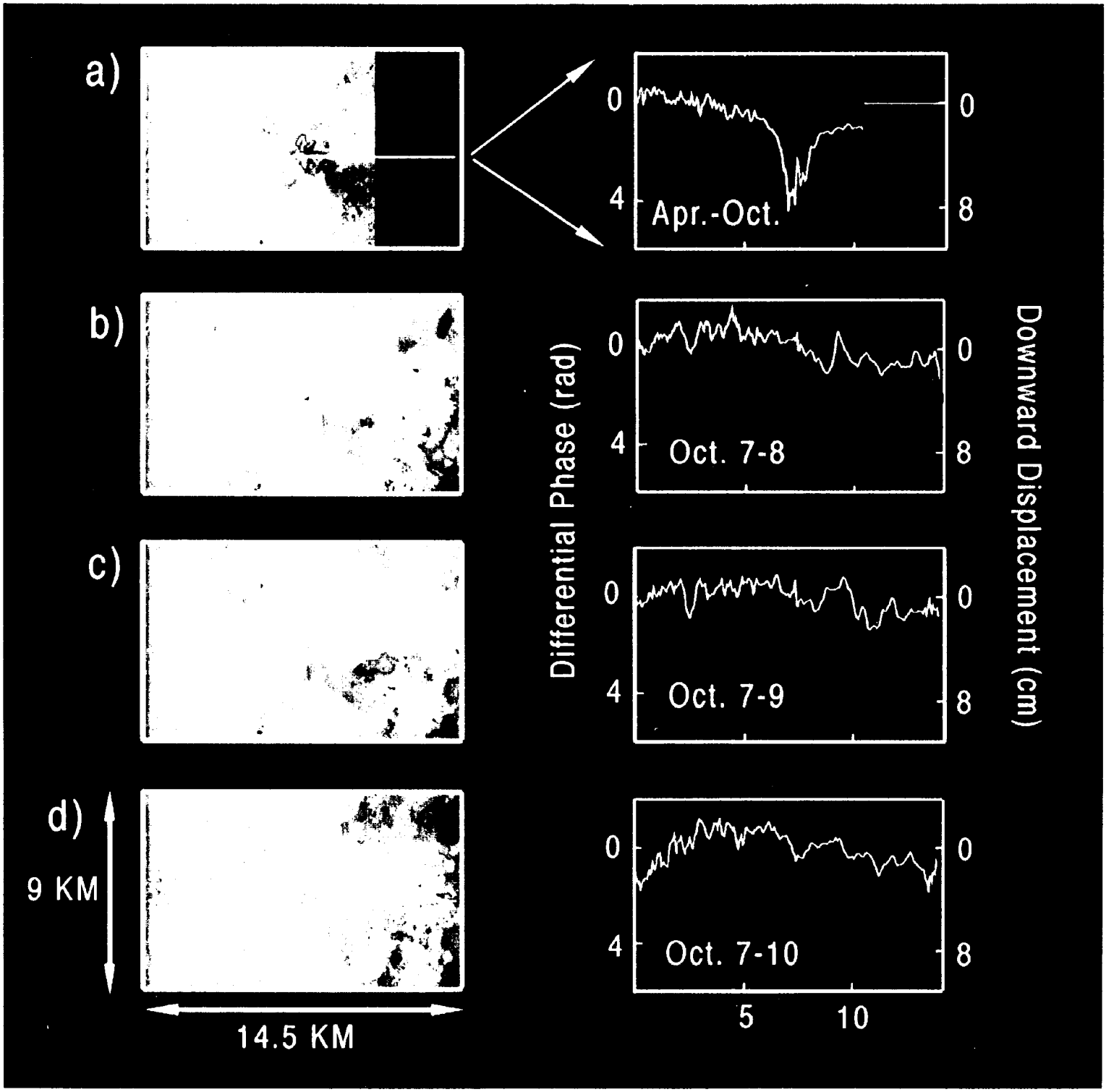

Figure 11 Rosen *et al.*

Surface deformation and coherence measurements of Kilauea Volcano, Hawaii from SIR-C radar interferometry